

# Compact MHz high repetition rate EUV to soft x-ray free electron laser

Ji Qiang

*Lawrence Berkeley National Laboratory, Berkeley, CA 94720*

High-brightness X-ray Free Electron Lasers (FELs) produce spatially and temporally coherent pulses on attosecond to femtosecond timescales, providing a transformative tool for discovery across biology, chemistry, physics, and materials science. However, most existing FELs are kilometer-scale facilities with billion-dollar construction costs and low repetition rates (about 100 Hz), which limits their accessibility and scientific throughput. This paper proposes a compact, high-repetition-rate (MHz) EUV to 1 nm soft X-ray FEL with a footprint of less than 100 meters. Such an FEL is suitable for installation within university or research institution settings where space is limited. The facility leverages a multi-turn recirculating linear accelerator that integrates state-of-the-art superconducting accelerator technology with recent advances in diffraction-limited storage rings. We present the conceptual design and analyze the impact of incoherent and coherent synchrotron radiation, demonstrating that these effects are not limiting factors for achieving high-quality electron beams. Such a compact X-ray FEL facility would substantially reduce both construction and operational costs, greatly expanding access to these powerful research tools. Furthermore, the design provides a potential upgrade path to generating hard X-ray radiation by incorporating high accelerating gradient structures to further accelerate a portion of the MHz electron beam.

## I. INTRODUCTION

X-ray light sources are indispensable tools for high-resolution experimental studies across a vast range of scientific disciplines, from structural biology and chemistry to materials science. The scientific grand challenges that next-generation photon sources must address have been well-defined, notably by the Basic Energy Sciences Advisory Committee in its report on “Next Generation Photon Sources” [1]. These challenges demand the ability to probe two fundamental regimes: the temporal evolution of electronic, atomic, and chemical processes on femtosecond timescales, and the structural and spectroscopic imaging of nano-objects with nanometer spatial resolution.

X-ray Free Electron Lasers (FELs) are uniquely suited to meet these demands. Their attosecond-to-femtosecond pulse durations are ideal for studying ultrafast dynamics, while their spatial and temporal coherence enable imaging with unparalleled spatial and spectral resolution. Furthermore, FELs deliver brightness many orders of magnitude beyond that of conventional synchrotron radiation sources [2]. While emerging diffraction-limited storage rings also promise a significant increase in brightness over third-generation sources, they lack a critical capability for ultrafast science. Specifically, they do not possess temporal coherence, and their pulse durations of over 100 picoseconds are ill-suited for resolving the ultrafast dynamics central to many of today’s scientific questions.

The past two decades have seen the successful construction and operation of several pioneering X-ray FELs, including LCLS, FERMI, SACLA, PAL-XFEL, SwissFEL, SXFEL, and the European XFEL [3–9]. While scientifically transformative, most these facilities operate at a low repetition rate (100 Hz), which severely limits the number of available user beamlines (typically fewer than five) and contributes to high operational costs per experiment. To address these limitations, the global focus has shifted toward the development of high-repetition-rate (MHz) free electron lasers. This initiative will lead to the establishment of major new facilities including the soft/hard X-ray LCLS-II in the United States [10, 11] and a combined soft/hard X-ray FEL in China [12] in addition to the hard X-ray XFEL in Germany. Despite their advanced capabilities, these machines require kilometer-scale footprints and investments exceeding one billion dollars. For instance, the recently commissioned LCLS-II operates at 4 GeV, with plans for an upgrade to 8 GeV to generate shorter wavelength X-rays, and spans over three kilometers in length. Similarly, other proposed next-generation MHz facilities, such as MariX, are designed with substantial footprints of approximately 500 meters [13]. The considerable scale and cost of these high-repetition-rate FELs highlight the need for a more compact and cost-effective design.

The pursuit of compact X-ray FELs is an active area of research, with several concepts proposed or under construction [14–16]. These designs primarily rely on high-gradient, normal-conducting C-band or X-band RF structures to achieve a smaller footprint. However, this approach has a limitation: it is fundamentally unsuited for the MHz-class repetition rates required for next-generation experiments. To overcome this challenge, this paper introduces a novel design for a compact EUV to soft X-ray FEL facility with the potential to divert a fraction of the MHz electron beam to drive a hard-X-ray FEL. Our approach is based on superconducting radio-frequency (SRF) accelerating cavities, a technology inherently capable of supporting MHz repetition rates, combined with a recirculating linear accelerator (linac) architecture, thereby uniting the goals of high throughput with a dramatically reduced facility footprint.

Recirculating linear accelerators have been proposed for X-ray FELs in previous studies [17–20]. Compared to those

concepts, the compact XFEL facility presented in this paper features a significantly smaller footprint and employs several novel techniques: (1) folding the low-emittance electron beam injector into the transverse dimension to reduce the total footprint; (2) using two superconducting linacs positioned on opposite sides of the recirculating linac for three-pass acceleration of the electron beam to nearly 2 GeV; (3) replacing the traditional 180-degree return arcs with two 90-degree arcs separated by straight transfer line sections dedicated to beam diagnostics, manipulation, heating, seeding, and path length control; (4) adopting the compact multi-bend achromat (MBA) design from diffraction-limited synchrotron light sources to preserve small transverse emittances; (5) utilizing 90-degree arcs for initial modest bunch compression to maintain electron beam quality, followed by a large bunch compressor for final compression to achieve kilo-Ampere peak currents; and (6) employing a passive dechirper after final compression to reduce the correlated energy spread of the electron beam. Together, these techniques enable the generation of the high-brightness electron beam required for the proposed compact XFEL facility.

The organization of this paper is as follows: Following the Introduction, we present the compact high-repetition-rate X-ray FEL facility concept in Section 2, study the potential emittance growth due to Incoherent Synchrotron Radiation (ISR) and Coherent Synchrotron Radiation (CSR) in Section 3, and discuss potential challenges and future work in Section 4.

## II. A COMPACT HIGH REPETITION RATE X-RAY FEL FACILITY

Current X-ray FEL facilities worldwide utilize straight RF linear accelerators to generate high-brightness electron beams, which subsequently pass through an undulator to produce coherent X-ray radiation. In this paper, we propose a novel compact recirculating RF accelerator as an alternative to the conventional straight linear accelerator, which typically spans several hundred to thousands of meters. This innovative design significantly reduces the facility's footprint. Additionally, the recirculating accelerator decreases the number of required RF cavities and enhances both RF and cooling efficiency. Consequently, the compact X-ray FEL offers a more cost-effective solution. Furthermore, to achieve compactness in this new design, we propose dividing each 180-degree arc into two 90-degree arcs separated by a straight section. These straight sections accommodate beam diagnostics and manipulation, laser heaters, and even external seeding. The photoinjector is also integrated into a straight section to further minimize the accelerator's length. Compact multi-bend achromats are employed for the 90-degree arcs. Beyond compactness, the recirculating architecture mitigates the transport of dark current into the undulator, offering an advantage over straight linear accelerators.

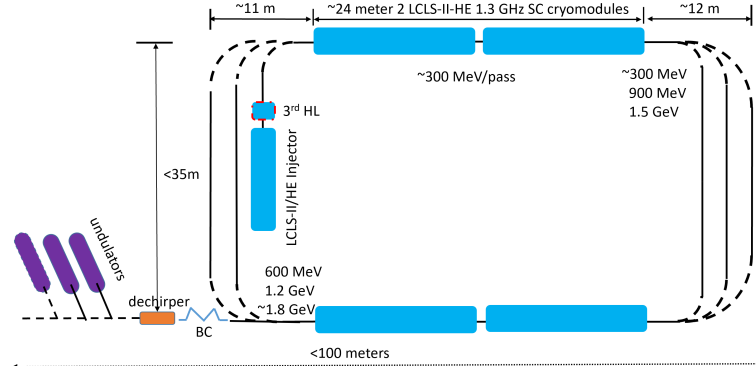


FIG. 1: Schematic plot of the compact x-ray FEL facility.

A layout of the compact X-ray FEL is shown in Fig. 1. It consists of a high-repetition-rate LCLS-II/HE-type injector, a 3.9 GHz third-harmonic linearizer, a 90-degree achromatic arc, a 4-meter matching section, and two cryomodules comprising 16 1.3 GHz superconducting cavities designed for LCLS-II/HE [21]. The layout further includes a second 4-meter matching section, three additional 90-degree achromatic arcs, three straight transfer lines, another set of three 90-degree achromatic arcs, a third 4-meter matching section, two more superconducting cavity cryomodules, another matching section, two additional 90-degree achromatic arcs, two straight transfer lines, another pair of 90-degree achromatic arcs, a bunch compressor (BC), a passive longitudinal dechirper, switch kickers, and a farm of FEL undulators. The longitudinal height of the outermost arc on the right side is approximately 8 meters, while the longitudinal height of the outermost arc on the left side is approximately 7 meters. The length of each of the two superconducting cryomodules is about 24 meters, based on the LCLS-II design. This results in a total length for the electron accelerator of less than 50 meters.

A 100 pC electron beam from the high-repetition-rate injector exhibits a peak current of approximately 10 A [22]. A third-harmonic superconducting cavity module is employed to control or linearize the longitudinal phase space downstream. After this module, the electron beam achieves an energy of about 50 to 80 MeV. This beam is then transported through the first top-left 90-degree achromatic arc into the top superconducting linac section. The maximum accelerating gradient of the 1.3 GHz superconducting cavity is assumed to be 20 MV/m, as utilized in the LCLS-II HE project.

After acceleration in the top superconducting linac, the electron beam reaches an energy of about 300 MeV. It is subsequently transported through the first top-right 90-degree achromatic arc into a straight transfer line, where beam diagnostics and a laser heater can be installed. Following this transfer line, the beam passes through the first bottom-right 90-degree achromatic arc and enters the bottom superconducting linac section, which employs the same type of RF cavities as the top linac. After acceleration in this linac, the beam attains an energy of approximately 600 MeV.

The beam is then transported through a series of arcs and transfer lines, including the first bottom-left 90-degree achromatic arc, the first left straight transfer line, and the second top-left 90-degree achromatic arc, before re-entering the top superconducting linac. After this second pass, the beam reaches an energy of about 900 MeV. It is subsequently transported through the second top-right 90-degree achromatic arc, another straight transfer line, and the second bottom-right 90-degree achromatic arc before entering the bottom superconducting linac for the second time, achieving an energy of 1.2 GeV.

This process continues with the beam passing through the second bottom-left 90-degree achromatic arc, the second left straight transfer line, and the third top-left 90-degree achromatic arc to enter the top linac for the third time. After this acceleration, the beam attains an energy of approximately 1.5 GeV. It is then transported through the third top-right 90-degree achromatic arc, the third right transfer line, and the third bottom-right 90-degree achromatic arc before entering the bottom superconducting linac for the third time, reaching a final energy of about 1.8 GeV.

Finally, the electron beam is extracted from the recirculating superconducting linac and undergoes final compression in a bunch compressor, achieving a peak current of approximately 1 kA. The chirp in the electron beam after compression is removed using a passive dechirper [23–25] before the beam is directed into X-ray FEL undulators to produce coherent X-ray radiation.

The performance of the X-ray FEL radiation can be estimated using the electron beam from the compact recirculating linac described above and the analytical model in reference [26]. The resonant equation for X-ray FEL coherent radiation is given by:

$$\lambda_r = \frac{\lambda_u}{2\gamma^2} \left( 1 + \frac{K_0^2}{2} \right) \quad (1)$$

where  $\lambda_r$  is the radiation wavelength,  $\lambda_u$  is the undulator period,  $\gamma$  is the relativistic factor of the electron beam, and  $K_0$  is the undulator parameter. For a 1 nm soft X-ray radiation with an undulator period of 15 mm, the undulator parameter is calculated to be 1.14.

An important parameter influencing X-ray FEL radiation performance is the FEL parameter  $\rho$ , defined as:

$$\rho = \left[ \frac{1}{16} \frac{I_e}{I_A} \frac{K_0^2 [JJ]^2}{\gamma^3 \sigma_x^2 k_u^2} \right]^{1/3} \quad (2)$$

where  $I_e$  is the electron peak current,  $I_A \approx 17$  kA is the Alfvén current,  $[JJ] = J_0(\xi) - J_1(\xi)$  with  $J_0$  and  $J_1$  being the 0th- and 1st-order Bessel functions, respectively, and  $\xi = K_0^2/(4 + 2K_0^2)$ , and  $k_u = 2\pi/\lambda_u$  is the wave number associated with the undulator period. Assuming a final electron beam normalized emittance of 0.5 mm mrad and an average Twiss beta function of 10 m, the FEL parameter is  $\rho = 7 \times 10^{-4}$ . For emittances of 1 mm mrad and 2 mm mrad, the values are  $\rho = 5.6 \times 10^{-4}$  and  $\rho = 4.4 \times 10^{-4}$ , respectively.

The saturation power of the X-ray FEL radiation depends on the FEL parameter and is approximated by:

$$P_{sat} \approx \rho \frac{E_e I_e}{e} \quad (3)$$

For the aforementioned FEL parameters, the corresponding saturation powers are approximately 1.3 GW, 1.0 GW, and 0.8 GW for the three emittance values, respectively.

The X-ray FEL power gain length is given by:

$$L_{G0} = \frac{\lambda_u}{4\pi\sqrt{3}\rho} \quad (4)$$

For the three final emittance values, the corresponding gain lengths are 0.99 m, 1.23 m, and 1.57 m, respectively. Typically, it requires approximately 20 gain lengths for the coherent X-ray radiation to reach saturation, resulting

in undulator lengths of 20 m, 24 m, and 32 m, respectively. Accounting for gaps between undulator sections, the maximum undulator hall length is expected to be less than 50 m.

Combining the undulator hall length with the less than 50 m length of the recirculating superconducting linac, the total length of the X-ray FEL facility is less than 100 m. This compact footprint makes the facility suitable for installation in space-constrained universities or research institutions.

To produce effective coherent X-ray radiation in the FEL, the final electron beam emittance should satisfy the following condition:

$$\epsilon_n < \gamma \frac{\lambda_r \bar{\beta}}{4\pi L_{G0}} \quad (5)$$

Using the gain lengths and the average Twiss beta function value discussed above, this results in  $\epsilon_n < 2.8$  mm mrad,  $\epsilon_n < 2.3$  mm mrad, and  $\epsilon_n < 1.8$  mm mrad for the respective cases. The first two conditions are clearly satisfied for the assumed final emittances of 0.5 mm mrad and 1 mm mrad. However, the assumed emittance of 2 mm mrad is near the boundary. This suggests that, for effective X-ray FEL radiation, the final electron beam emittance from the recirculating linac should be less than 2 mm mrad.

In the preceding discussion, we have demonstrated that an electron beam with an energy of 1.8 GeV, a peak current of 1 kA, and a transverse emittance of less than 2 mm mrad can produce GW-level coherent X-ray radiation at 1 nm within a 50 m undulator hall. In the following sections, we discuss how to achieve these final electron beam parameters.

We begin with considerations of longitudinal beam dynamics. A final compression factor of 10 to 20 is assumed, which must be achieved through over-compression due to the positive energy chirp of the electron beam before the final bunch compressor. This positive energy chirp is necessary to compress the electron beam using the 90-degree achromatic arcs, which have negative  $R_{56}$  values. For the same absolute compression value but with over-compression, the final relative energy chirp  $h_f = \frac{d(\Delta\gamma_f/\gamma_f)}{dz_f}$  of the electron beam before compression is given by:

$$h_f = -\frac{1}{R_{56f}} \left( 1 + \frac{1}{|C_f|} \right) \quad (6)$$

where  $R_{56f}$  is the momentum compaction factor of the last bunch compressor, and  $C_f$  is the final bunch compression factor. Assuming  $R_{56f} = -0.2$  m and a final compression factor of 10 to 20, the final relative energy chirp should range from  $5.25 \text{ m}^{-1}$  to  $5.5 \text{ m}^{-1}$ .

For the proposed recirculating linac shown in Fig. 1, the final energy deviation can be expressed as:

$$\Delta\gamma_f = \left( h_0\gamma_0 \prod_{i=1}^6 C_i + \bar{V}_1 k \sin \phi_1 \sum_{j=1}^3 \prod_{i=2j}^6 C_i + \bar{V}_2 k \sin \phi_2 \sum_{j=1}^2 \prod_{i=2j+1}^6 C_i + \bar{V}_2 k \sin \phi_2 \right) z_f \quad (7)$$

where  $h_0$  is the initial relative energy chirp after the third-harmonic linearizer,  $C_i$  is the compression factor after arc  $i$  (with the first arc being the top-left 90-degree achromatic arc after the linearizer),  $\bar{V}_1$  and  $\bar{V}_2$  are the normalized voltages of the top and bottom superconducting linacs, respectively,  $\phi_1$  and  $\phi_2$  are the design phases of the top and bottom linacs, respectively, and  $k$  is the wave number corresponding to the RF frequency.

Assuming both top and bottom linacs operate at the same voltage  $\bar{V}$  and phase  $\phi$ , all arcs except the first have the same compression factor  $C$ , and neglecting the initial energy chirp, the final energy deviation simplifies to:

$$\Delta\gamma_f = \bar{V} k \sin \phi \frac{C^6 - 1}{C - 1} z_f \quad (8)$$

The final relativistic factor  $\gamma_f$  after three acceleration passes, neglecting the initial energy, is:

$$\gamma_f = 6\bar{V} \cos \phi \quad (9)$$

The resulting final relative energy chirp is then:

$$h_f = k \tan \phi \frac{C^6 - 1}{6(C - 1)} \quad (10)$$

In this proposed facility, the final peak current is approximately 1 kA. Given a compression factor of 10 to 20 in the last bunch compressor, the electron beam peak current before final compression should be between 50 A and 100 A. With an initial peak current of 10 A from the injector, the total compression factor through the five major arcs (including straight sections) should be between 5 and 10. This implies a compression factor per arc of 1.38 to 1.59. Using Eq. 10, this corresponds to an RF phase of approximately 2.70 to 4.25 degrees for the superconducting linac to achieve a chirp of  $5.25 \text{ m}^{-1}$  to  $5.5 \text{ m}^{-1}$ . These RF design phases have minimal impact on the final achievable electron beam energy.

### III. EFFECTS OF ISR AND CSR IN ARCS

In the recirculating superconducting electron linac described above, multiple 90-degree achromatic arcs are employed. Leveraging recent advances in diffraction-limited synchrotron light source storage ring design, in this study, we propose to use a multi-bend achromat (MBA) system to minimize emittance growth [27]. A schematic plot of the MBA system is shown in Fig. 2.

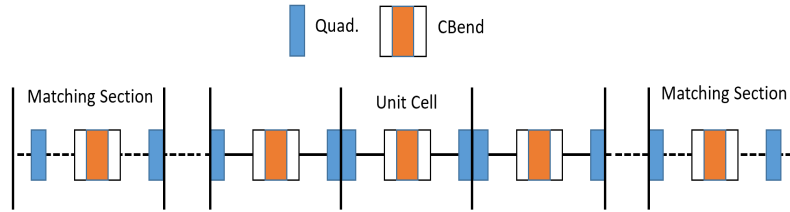


FIG. 2: Schematic layout of a multi-bend achromat 90-degree arc.

This MBA lattice consists of a number of periodic cells, each comprising a combined-function bending magnet, two drift spaces, and two half-quadrupoles, along with two matching cells on either side of the periodic cells. In this study, the two matching cells are assumed to be identical, each containing a combined-function bending magnet, a drift space, and a quadrupole. It is further assumed that the combined-function bending magnet in the matching cell is identical to that in the periodic cells, and the quadrupole in the matching cell has the same strength as the quadrupoles in the periodic lattice.

To achieve an achromatic multi-bend arc, the drift length  $L_d$  between the bending magnet and quadrupole in the matching cell, as well as the quadrupole length  $L_q$ , can be determined as follows. Assuming the linear transfer matrix through the periodic cells is denoted by  $R$ , the periodic dispersion and its derivative at the end of the cells can be obtained by solving the following equation:

$$\begin{pmatrix} D \\ D' \\ 1 \end{pmatrix} = \begin{pmatrix} R_{11} & R_{12} & R_{16} \\ R_{21} & R_{22} & R_{26} \\ 0 & 0 & 1 \end{pmatrix} \begin{pmatrix} D \\ D' \\ 1 \end{pmatrix} \quad (11)$$

The solution of the above equation results in:

$$\begin{pmatrix} D \\ D' \end{pmatrix} = \frac{1}{2 - R_{11} - R_{22}} \begin{pmatrix} (1 - R_{22})R_{16} + R_{12}R_{26} \\ R_{21}R_{16} + (1 - R_{11})R_{26} \end{pmatrix} \quad (12)$$

These dispersions are set to zero outside two matching cells to form an achromat arc by selecting the appropriate drift length and quadrupole length in the matching cells as follows:

$$L_q = \frac{1}{\sqrt{K_q}} \arcsin \left( \frac{R_{26}^b}{D\sqrt{K_q}} \right), \quad (13)$$

$$L_d = -\frac{R_{16}^b}{R_{26}^b} - \frac{R_{22}^q}{R_{21}^q}, \quad (14)$$

where  $R_{21}^q$  and  $R_{22}^q$  are the linear transfer matrix elements of the quadrupole, and  $R_{16}^b$  and  $R_{26}^b$  are the linear transfer matrix elements of the combined-function bending magnet.

As an illustration, Fig. 3 shows the evolution of the Root Mean Square (RMS) beam size and emittance of an electron beam through an 11-bend, 90-degree achromat arc. The dipole field within the 0.457-meter-long bending magnet is 1.25 T. In the periodic cell, the length of the focusing quadrupole is 0.2 m, and the separation between the quadrupole and the combined-function bend is also 0.2 m. The height of this arc is approximately 7 m, and the width is approximately 8 m.

In this example, the electron beam energy is 1.2 GeV. No collective effects are included in the simulation; only a linear transfer map was used for tracking. The initial electron beam distribution is transversely matched to the periodic cells and has an initial longitudinal relative energy chirp of  $2 \text{ m}^{-1}$ . The horizontal phase advance per cell within the periodic cells is 69 degrees, and the vertical phase advance is 47 degrees. There is a slight mismatch throughout the entire lattice. The defocusing quadrupole within the combined-function bend has a strength of  $K = -5/\text{m}^2$ , while

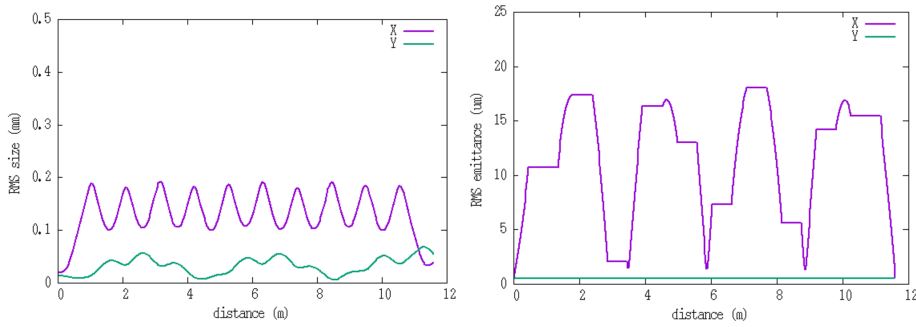


FIG. 3: Electron beam RMS size evolution (left) and emittance evolution (right) through a 90-degree, 11-bend achromat arc with a beam energy of 1.2 GeV and zero current.

the focusing quadrupole has a strength of  $k = 12.65/m^2$ . In the matching cells, the drift length is  $L_d = 0.48$  m, and the quadrupole length is  $L_q = 0.11$  m.

The horizontal RMS size is dominated by regular dispersion oscillations, which exhibits a minimum inside the bending magnet. The vertical RMS size shows some mismatch. However, with the linear transfer map, the emittance after the arc returns to its initial value of  $0.5 \mu\text{m}$ . There is no emittance growth due to dispersion, thanks to the achromat design.

The Incoherent Synchrotron Radiation (ISR) contributes to the growth of uncorrelated energy spread. An analytical estimate of the energy spread increase in eV through a 180-degree arc is given by [28]:

$$\sigma_E = \frac{\sqrt{0.118\gamma^7}}{\rho} \times 10^{-7}, \quad (15)$$

where  $\rho$  is the bending radius. For a 1.5 GeV electron beam passing through an arc with a 4-meter bending radius under a 1.25 T magnetic field strength within the bend, this results in an energy spread of approximately 12 keV. For a 1.2 GeV electron beam passing through the same magnetic field arc, the energy spread is approximately 7 keV. This increase in energy spread due to ISR was also verified using the Fokker-Planck model in reference [29]. We measured the final uncorrelated energy spread growth through an 11-bend, 90-degree arc at 1.2 GeV as approximately 5 keV and at 1.5 GeV as approximately 9 keV. The simulation results agree well with the analytical estimates after taking into account the contribution from another 90-degree arc. The total ISR contribution to the uncorrelated energy spread across eleven arcs is expected to be less than 20 keV.

The normalized emittance growth due to quantum excitation from ISR through a 180-degree arc can also be estimated as [28]:

$$\Delta\epsilon_n = 7.19 \times 10^{-28} \frac{\gamma^6}{\rho^2} \langle H \rangle, \quad (16)$$

where  $\langle H \rangle$  is related to the Twiss beta function and dispersion inside the bend. For a 1.5 GeV beam passing through an arc with a 4-meter bending radius and  $\langle H \rangle = 1$  m, this results in a normalized emittance growth of approximately  $0.03 \mu\text{m}$ . For a 1.2 GeV electron beam through an arc with a 3.2 m bending radius, the ISR-induced emittance growth is approximately  $0.01 \mu\text{m}$ . This suggests that the ISR effects in the proposed multi-bend achromat arcs are negligible. This conclusion is also supported by the macroparticle simulations discussed below.

The effects of Coherent Synchrotron Radiation (CSR) on normalized beam emittance growth through a bending magnet can be estimated by including contributions from both the longitudinal and transverse components of the CSR field as [30]:

$$\Delta\epsilon_{n,L} = 7.5 \times 10^{-3} \frac{\beta_T}{\gamma} \left( \frac{r_e N L_B^2}{\rho^{5/3} \sigma_z^{4/3}} \right)^2, \quad (17)$$

$$\Delta\epsilon_{n,T} = 2.5 \times 10^{-2} \frac{\beta_T}{\gamma} \left( \frac{r_e N L_B}{\rho \sigma_z} \right)^2, \quad (18)$$

where  $\beta_T$  is the average bend-plane betatron function in the dipole magnet,  $\gamma$  is the relativistic Lorentz factor for the beam's mean energy,  $r_e$  is the classical electron radius,  $N$  is the number of electrons in the beam,  $L_B$  is the length of the bending magnet,  $\rho$  is the bending radius of the magnet, and  $\sigma_z$  is the RMS bunch length. For an electron

beam with a charge of approximately 100 pC and an RMS bunch length of approximately 0.7 mm (corresponding to a peak current of about 10 A), using a 1.25 T dipole magnet and assuming  $\beta_T = 10$  m inside the dipole magnet, the normalized emittance growth through a 90-degree arc is approximately  $0.0004 \mu\text{m}$  with 11 dipoles,  $0.0007 \mu\text{m}$  with 9 dipoles, and  $0.001 \mu\text{m}$  with 7 dipoles for a 1.2 GeV electron beam. For a 1.5 GeV electron beam, the growth is approximately  $0.001 \mu\text{m}$  with 7 dipoles,  $0.0006 \mu\text{m}$  with 9 dipoles, and  $0.0004 \mu\text{m}$  with 11 dipoles. Using more dipole magnets for a 90-degree arc results in reduced emittance growth.

Further increasing the electron beam peak current by reducing the RMS bunch length by a factor of 10 (corresponding to a peak current of approximately 100 A) results in significantly larger CSR-induced emittance growth. For a 1.2 GeV electron beam, the normalized emittance growth after a 7-dipole, 90-degree arc is approximately  $0.5 \mu\text{m}$ , about  $0.2 \mu\text{m}$  after a 9-dipole arc, and about  $0.1 \mu\text{m}$  after an 11-dipole, 90-degree arc. The results are comparable for a 1.5 GeV electron beam. While these emittance growth values are significant, they are not unacceptable. This suggests that the electron beam peak current should be kept below 100 A and that more bending magnets should be used to mitigate CSR-induced emittance growth.

Next, we evaluate the effects of element nonlinearity by using an exact model for drift, incorporating energy dependence in the quadrupole, employing a fifth-order transfer map for the bending magnet, and considering the effects of ISR, one-dimensional CSR, and space-charge using particle tracking. These evaluations are conducted for the same electron beam as described above, but with an initial peak current of 60 A. Figure 4 shows the RMS size and emittance evolution through the arc, obtained from macroparticle simulations that include all the aforementioned effects, performed using the parallel beam dynamics code IMPACT [31, 32].

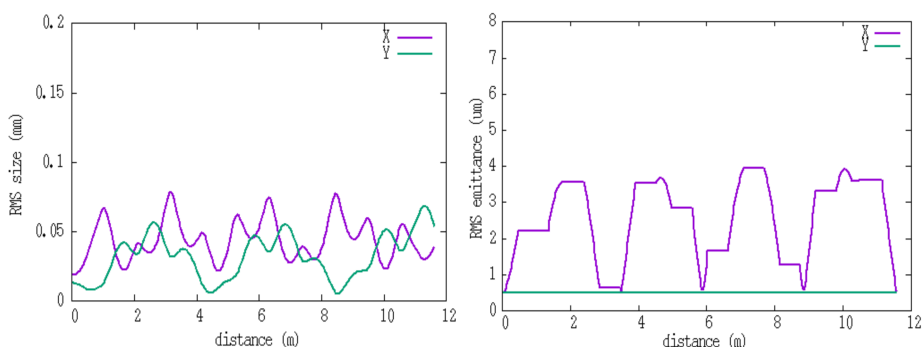


FIG. 4: Electron beam RMS size evolution (left) and emittance evolution (right) through a 90-degree, 11-bend achromat arc with a beam energy of 1.2 GeV and an initial peak current of 60 A.

With the 60 A peak current, the transverse sizes are mismatched. The emittance evolution exhibit patterns similar to those observed in the zero-current case discussed earlier. However, there is a slight final horizontal emittance growth of approximately 5%, with the dominant contribution of about 3% arising from lattice element nonlinearity.

In order to systematically evaluate the collective effects (primarily from CSR), we measured the final emittance growth after the arc for different initial peak currents with two initial emittances of  $0.5 \mu\text{m}$  and  $1 \mu\text{m}$ . We also studied the emittance growth using 7, 9, and 11 combined-function bends in a 90-degree arc, maintaining the same separation distance between consecutive bends. For a 1.2 GeV electron beam, the results are summarized in Fig. 5.

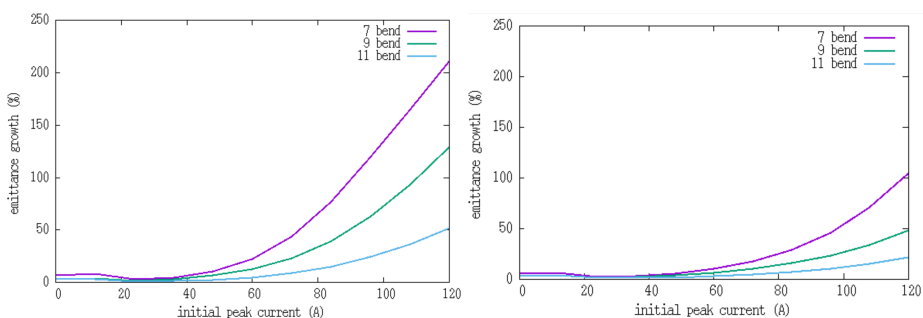


FIG. 5: Horizontal emittance growth through 7-bend, 9-bend, and 11-bend achromat arcs with an initial emittance of  $0.5 \mu\text{m}$  (left) and  $1 \mu\text{m}$  (right) at a beam energy of 1.2 GeV.

Across the range of initial peak currents studied, the emittance growth in the 7-bend arc is consistently higher than

in the 9-bend and 11-bend arcs. Moreover, using more bending magnets in the arc results in smaller final emittance growth at the end of the arc. This may be attributed to the fact that a greater number of bending magnets leads to faster focusing and a smaller horizontal beam size within the bend, thereby reducing CSR-induced emittance growth. The final emittance growth through the 11-bend achromat arc can be kept below 10% for initial peak currents below 70 A. To achieve a final emittance growth of less than 10%, the initial peak current in the 9-bend arc should be less than 50 A, and less than 40 A in the 7-bend arc. With a larger initial emittance, the final emittance growth is reduced, though the basic trend remains unchanged. Using fewer bending magnets in a 90-degree arc reduces construction costs and the arc height (and thus the footprint), but it also increases the risk of larger emittance growth.

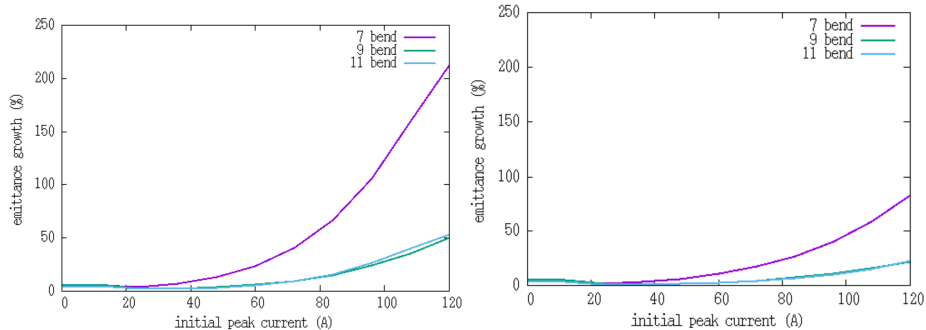


FIG. 6: Horizontal emittance growth through 7-bend, 9-bend, and 11-bend achromat arcs with an initial emittance of  $0.5 \mu\text{m}$  (left) and  $1 \mu\text{m}$  (right) at a beam energy of 1.5 GeV.

We also measured the emittance growth as a function of initial peak current for an electron beam passing through 7-bend, 9-bend, and 11-bend arcs at a beam energy of 1.5 GeV. The simulation results are shown in Fig. 6. The emittance growth at this energy exhibits a similar pattern to the case at 1.2 GeV, except for a lower emittance growth through the 9-bend achromat arc. The emittance growth can be kept below 10% for peak currents up to 70 A in the 9-bend and 11-bend arcs, and below 40 A for the 7-bend arc.

In all three bending magnet arcs, the vertical emittance growth at the end of the arc is small (less than 1%).

In the above 90-degree arc, the separation between two bending magnets is assumed to be 0.6 m. This might be too tight for magnet hardware installation. We remeasured the emittance growth assuming a separation of 0.7 m between bending magnets in the 11-bend arc at 1.5 GeV. Figure 7 shows the final emittance growth as a function of initial peak current with an initial emittance of  $0.5 \mu\text{m}$ .

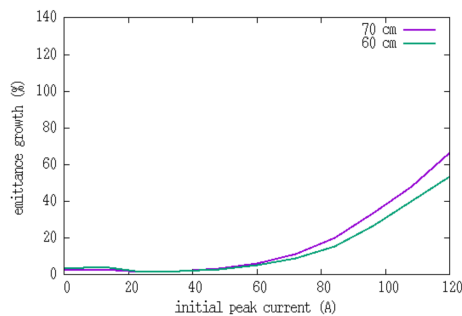


FIG. 7: Horizontal emittance growth through an 11-bend achromat arc with a 0.7 m separation between bending magnets, an initial emittance of  $0.5 \mu\text{m}$ , and a beam energy of 1.5 GeV.

It is seen that there is slightly greater emittance growth across the initial current range with this larger separation. However, the final emittance growth can still be kept below 10% for initial peak currents below 70 A. Increasing the separation between bending magnets would result in an increase in the arc height by approximately 0.5 m.

We also considered a case with a weaker magnetic field. In the above arcs, the magnetic field strength inside the bending magnet is assumed to be 1.25 T. We investigated a weaker magnetic field case with a strength of 1 T inside the bending magnet. This results in a larger bending radius and a longer bending magnet length. Consequently, the arc height increases by approximately 1 m at 1.5 GeV. We remeasured the emittance growth assuming a 1 T magnetic field inside the bending magnets and a 0.6 m separation between them in the 11-bend arc at 1.5 GeV beam energy. Figure 8 shows the final emittance growth as a function of initial peak current with an initial emittance of  $0.5 \mu\text{m}$ .

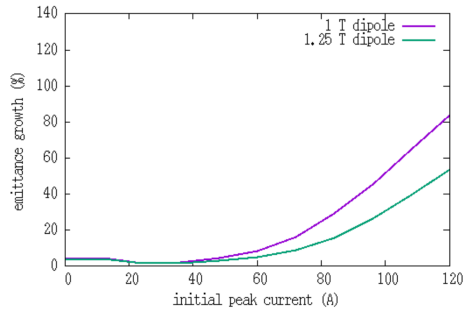


FIG. 8: Horizontal emittance growth through an 11-bend achromat arc with a 1 T magnetic field, an initial emittance of  $0.5 \mu\text{m}$ , and a beam energy of 1.5 GeV.

There is slightly greater emittance growth across the initial current range with this weaker magnetic field inside the bends. Nevertheless, the final emittance growth can be kept below 10% for most initial peak currents below 60 A.

There are a total of eleven 90-degree arcs in the proposed recirculating linac. With a 10% emittance growth through each arc, this results in less than a factor of 3 growth in emittance from the injector. Based on the LCLS-II-HE injector design, an emittance of  $0.1 \mu\text{m}$  can be achieved with a peak current of approximately 10 A [33, 34]. This suggests that the emittance through the recirculating linac (after the eleven arcs) and before the final compression can be less than  $1 \mu\text{m}$ . Assuming the emittance growth after the final compression (by a factor of 10–20) is less than 100%, the electron beam after the final bunch compression can achieve a peak current of 1 kA with an emittance of less than  $2 \mu\text{m}$ .

#### IV. CONCLUSION AND DISCUSSION

In this paper, we propose a compact, MHz high-repetition-rate facility for extreme ultraviolet to soft X-ray free electron laser radiation. Based on a recirculating superconducting linear accelerator, the design features a footprint of less than 100 meters and utilizes five cryomodules similar to those in LCLS-II-HE, each containing eight 1.3 GHz superconducting RF cavities.

With an appropriate choice of peak beam current, incoherent synchrotron radiation and coherent synchrotron radiation in the eleven  $90^\circ$  achromatic arcs are not expected to be limiting factors. These do not induce significant horizontal emittance growth, and their impact on vertical emittance remains minimal.

The final 100 pC electron beam energy is approximately 1.8 GeV, with an energy spread of less than 500 keV, a peak current exceeding 1 kA, and a projected normalized emittance below  $2 \text{ mm}\cdot\text{mrad}$ . This electron beam can be directed to a farm of undulators to generate GW-level 1 nm X-ray radiation via either Self-Amplified Spontaneous Emission (SASE) or a seeded FEL. A portion of the 1 MHz electron beam can be diverted to a separate beamline and post-accelerated to nearly 10 GeV using high-gradient acceleration technologies, such as X-band or cryo-cooled C-band structures [35] or wakefield accelerators [36]. This high-energy beam can then be utilized to generate hard X-ray FEL radiation.

Several challenges remain in the development of this compact FEL facility, including the design of four merging sections for entering and exiting the arcs, longitudinal phase space control, microbunching instability mitigation, multi-bunch beam breakup instability suppression, and optimization of the final bunch compressor design.

The electron beam exiting the superconducting linac has different energies during each pass. This energy variation complicates the use of a single quadrupole lattice to match the beam into the two or three multi-bend achromat (MBA) arcs. This challenge can be addressed by extending the length of either the entrance or exit matching sections of the MBA. Following the first dipole magnet, beams with different energies enter energy-specific matching sections before proceeding to the periodic cells. These matching sections are individually designed to accommodate the specific beam energies and ensure proper matching of the Twiss parameters to the periodic cells.

In our preliminary design layout, sextupole magnets have not yet been incorporated. However, in addition to the third harmonic cavities located upstream of the first 90-degree arc, sextupole magnets can be implemented to control the longitudinal phase space effectively and to reduce emittance growth [37].

Microbunching instability represents a significant challenge in X-ray FEL accelerators, as it can substantially degrade the final electron beam quality [38, 39]. Several mitigation strategies are available, including installing a laser heater in the first straight section [40] or incorporating low-beta quadrupole lattices to exploit intrabeam scattering for beam heating [41]. Additionally, controlled dispersion leakage from the arcs can be utilized to suppress microbunching

instability [42, 43].

Within the recirculating superconducting linac, the electron beam traverses the superconducting cavities multiple times. It is crucial to suppress beam breakup instability arising from higher-order modes (HOMs) excited when off-axis beams pass through the RF cavities. This instability can be mitigated through specialized optics designs or the implementation of HOM dampers [44–46].

The design of the final bunch compressor may utilize an arc compression system with sufficiently large  $R_{56}$  values [47–50].

In addition, future work includes the design of a passive dechirper, a beam switch yard, and FEL undulators. Once these components are finalized, comprehensive start-to-end simulations will be conducted to evaluate the overall FEL performance, including all collective effects. Prior to construction, detailed simulations incorporating machine imperfections, alignment errors, and beam steering corrections should be performed to validate the design robustness.

## ACKNOWLEDGEMENTS

This work was supported by the U.S. Department of Energy (DOE), Office of Science, Office of High Energy Physics, under Contract No. DE-AC02-05CH11231. Computational resources were provided by the National Energy Research Scientific Computing Center (NERSC), which is supported by the DOE Office of Science under the same contract number.

- 
- [1] [https://cdn.lanl.gov/files/next-generation-photon-sources-rpt\\_e3a38.pdf](https://cdn.lanl.gov/files/next-generation-photon-sources-rpt_e3a38.pdf)
  - [2] “Accelerator Physics for Future Light Sources,” A collection of reports from the workshop sponsored by the DOE BES held in Gaithersburg, Maryland Sept. 15-17, 2009.
  - [3] P. Emma, et al., First lasing and operation of an ångstrom-wavelength free-electron laser, *Nat. Photon.* 4 (2010) 641.
  - [4] E. Allaria, et al., Highly coherent and stable pulses from the FERMI seeded free-electron laser in the extreme ultraviolet, *Nat. Photon.* 6 (2012) 699.
  - [5] T Ishikawa et al., A compact X-ray free-electron laser emitting in the sub-ångström region, *Nat. Photon.* 6, 540 (2012).
  - [6] H.-S. Kang et al., Hard X-ray free-electron laser with femtosecond-scale timing jitter, *Nat. Photon.* 11, p. 708, (2017).
  - [7] C. Milne et al., SwissFEL: The Swiss x-ray free electron laser, *Appl. Sci.* 7, 720 (2017).
  - [8] Zhao, Z., Wang, D., Gu, Q., et al. (2017). SXFEL: a soft X-ray free electron laser in China. *Synchrotron Radiat. News* 30, 29–33, <https://doi.org/10.1080/08940886.2017.1386997>.
  - [9] W. Decking et al., A MHz-repetition-rate hard X-ray free-electron laser driven by a superconducting linear accelerator. *Nat. Photon.* 14, 391–397 (2020).
  - [10] T. O. Raubenheimer et al., LCLS-II: Status of the CW XRay FEL Upgrade to the SLAC LCLS Facility, in *Proceedings of the 2015 Free Electron Laser Conference*, Daejeon, Korea, (JACoW, Geneva, 2015), pp. 618-624.
  - [11] Y. T. Ding, LCLS-II commissioning and operation with high-repetition-rate CW FELs, in *Proceedings of the 16th International Particle Conference*, Taipei, Taiwan, p. 1710 (2025).
  - [12] Z. T. Zhao, H. Ding, B. Liu, Shanghai hard X-ray FEL facility progress status, in *Proceedings of the 15th International Particle Conference*, Nashville, TN, p. 967 (2024).
  - [13] L Serafini et al., Marix, an advanced mhz-class repetition rate x-ray source for linear regime time-resolved spectroscopy and photon scattering, *Nucl. Instrum. Meth. A*, 930:167–172, 2019.
  - [14] CompactLight. Available online: <http://www.compactlight.eu> (accessed on 1 October 2020).
  - [15] J. B. Rosenzweig et. al., “An ultra-compact x-ray free-electron laser”, *New J. Phys.* 22 (2020) 093067.
  - [16] <https://biodesign.asu.edu/cxfel/>
  - [17] J. N. Corlett et al., A recirculating linac-based facility for ultrafast x-ray science, *Proc. 2003 Particle Accelerator Conference (IEEE,2003)*, pp. 186–188.
  - [18] P. Williams et. al., “Recirculating Linac Free-Electron Laser Driver”, *Phys. Rev. ST Accel. Beams*, vol. 14, 050704, May 2011.
  - [19] R. York, “5 Upgradable to 25 keV Free Electron Laser Facility”, *Phys. Rev. ST Accel. Beams*, vol. 17, 010705, Jan. 2014.
  - [20] A. Bacci et al., Two-pass two-way acceleration in a superconducting continuous wave linac to drive low jitter x-ray free electron lasers, *Phys. Rev. Accel. Beams* 22, 111304 (2019).
  - [21] T. O. Raubenheimer, The LCLS-II-HE, a high energy upgrade of the LCLS-II, in *Proc. of FLS2018*, Shanghai, China, 2018.
  - [22] C.F. Papadopoulos, D. Filippetto, F. Sannibale, P. Emma, T. Raubenheimer, J. Schmerge, L. Wang, F. Zhou, RF injector beam dynamics optimization for LCLS-II, p. 1974, in *Proc. of IPAC2014*, Dresden, Germany, (2014).
  - [23] P. Emma et al., Experimental Demonstration of Energy-Chirp Control in Relativistic Electron Bunches Using a Corrugated Pipe, *Phys. Rev. Lett.* 112, 034801 (2014).

- [24] Z. Zhang, K. Bane, Y. Ding, Z. Huang, R. Iverson, T. Maxwell, G. Stupakov, and L. Wang, Electron beam energy chirp control with a rectangular corrugated structure at the Linac Coherent Light Source, *Phys. Rev. ST Accel. Beams* 18, 010702 (2015).
- [25] T. Pacey, Y. Saveliev, G. Xia, and J. Smith, Simulation studies for dielectric wakefield programme at CLARA facility, *Nucl. Instrum. Methods Phys. Res., Sect. A* 909, 261 (2018).
- [26] Z. Huang and K.-J. Kim, Review of X-ray free-electron laser theory, *Phys. Rev. Spec. Top. Accel. Beams* 10, 034801 (2007).
- [27] D. Einfeld, M. Plesko, J. Schaper, First multi-bend achromat lattice consideration, *J Synchrotron Radiat.* 2014 Sep;21(Pt 5):856-61. doi: 10.1107/S160057751401193X.
- [28] D. Douglass, Incoherent estimates for possibly coherent light sources, JLAB-TN-08-013 report, 2008.
- [29] J. M. Jowett, Introductory statistical mechanics for electron storage rings, SLAC-PUB-4033, 1986.
- [30] S. Di Mitri et al., Scaling of beam collective effects with bunch charge in the CompactLight free-electron laser, *Photonics* 2020, 7, 125;doi:10.3390/photonics7040125
- [31] J. Qiang, R. D. Ryne, S. Habib, and V. Decyk, An Object-Oriented Parallel Particle-In-Cell Code for Beam Dynamics Simulation in Linear Accelerators, *J. Comput. Phys.* 163, 434 (2000).
- [32] J. Qiang, R. D. Ryne, M. Venturini, A. A. Zholents, I. V. Pogorelov, High resolution simulation of beam dynamics in electron linacs for x-ray free electron lasers, *Phys. Rev. ST Accel. Beams*, 12, 100702 (2009).
- [33] J. Qiang, F. Ji, T. O. Raubenheimer, Beam dynamics optimization of a low emittance photoinjector without buncher cavities, p. 615, in *Proc. of 5th North American Particle Accel. Conf, Albuquerque, NM, USA, 2022.*
- [34] F. Ji, C. Adolphsen, R. Coy, L. Ge, C.E. Mayes, T.O. Raubenheimer, L. Xiao, J. Qiang, Beam Dynamics Studies on a Low Emittance Injector for LCLS-II-HE, p. 619, in *Proc. of 5th North American Particle Accel. Conf, Albuquerque, NM, USA, 2022.*
- [35] E. I. Simakov, V. A. Dolgashev, and S. G. Tantawi, Advances in high gradient normal conducting accelerator structures, *Nucl. Instrum. Methods Phys. Res. A: Accel. Spectrom. Detect. Assoc. Equip.*, vol. 907, pp. 221–230, 2018.
- [36] A. Zholents et al., A high repetition rate millimeter wavelength accelerator for an X-ray free-electron laser, *JINST* 20, P01023, (2025).
- [37] R. J. England, J. B. Rosenzweig, G. Andonian, P. Musumeci, G. Travish, and R. Yoder, Sextupole correction of the longitudinal transport of relativistic beams in dispersionless translating sections, *Phys. Rev. ST Accel. Beams* 8, 012801 (2005).
- [38] D. Ratner, C. Behrens, Y. Ding, Z. Huang, A. Marinelli, T. Maxwell, and F. Zhou, Time-resolved imaging of the microbunching instability and energy spread at the Linac Coherent Light Source, *Phys. Rev. ST Accel. Beams* 18, 030704 (2015).
- [39] J. Qiang, Y. Ding, P. Emma, Z. Huang, D. Ratner, T. O. Raubenheimer, F. Zhou, and M. Venturini, Start-to-end simulation of the shot-noise driven microbunching instability experiment at the Linac Coherent Light Source, *Phys. Rev. Accel. Beams* 20, 054402 (2017).
- [40] Z. Huang, M. Borland, P. Emma, J. Wu, C. Limborg, G. Stupakov, and J. Welch, Suppression of microbunching instability in the linac coherent light source, *Phys. Rev. ST Accel. Beams* 7, 074401 (2004).
- [41] J. Qiang, X-ray free electron laser linear accelerator without a laser heater, *Nuclear Instruments & Methods in Physics Research A* 1048, 167968 (2023).
- [42] J. Qiang, C. Mitchell, M. Venturini, Suppression of microbunching instability using bending magnets in FEL linacs, *Phys. Rev. Lett.*, vol. 111, 054801 (2013).
- [43] B. Li and J. Qiang, Mitigation of microbunching instability in x-ray free electron laser linacs, *Phys. Rev. Accel. Beams* 23, 014403 (2020).
- [44] Georg H. Hoffstaetter, Vladimir Litvinenko, Hywel Owen, Optics and beam transport in energy recovery linacs, *Nuclear Instruments and Methods in Physics Research A* 557 (2006) 345–353.
- [45] C. Tennant, Energy recovery linacs, in *Challenges and Goals for Accelerators in the XXI Century*, ed. by O. Bruning and S. Myers, 2016. <https://doi.org/10.1142/8635>
- [46] S. Glukhov, O. Boine-Frankenheim, M. Arnold, and C. Stoll, Regenerative multibunch beam breakup instabilities and countermeasures for a high-intensity electron accelerator and the superconducting Darmstadt linear electron accelerator, *Phys. Rev. Accel. Beams* 25, 024402 (2022).
- [47] S. Di Mitri and M. Cornacchia, Transverse emittancepreserving arc compressor for high-brightness electron beam-based light sources and colliders, *Europhys. Lett.* 109, 62002 (2015).
- [48] J. A. G. Akkermans, S. Di Mitri, D. Douglas, and I. D. Setija, Compact compressive arc and beam switchyard for energy, *Phys. Rev. Accel. Beams* 20, 080705, 2017.
- [49] P. H. Williams, G. P´erez-Segurana, I. R. Bailey, S. Thorin, B. Kyle, and J. B. Svensson, Arclike variable bunch compressors, *Phys. Rev. Accel. Beams* 23, 100701 (2020).
- [50] A. Dixon, P. Williams, S. Thorin, T. Charles, A. Wolski, Reduction of arrival time jitter or energy spread with arclike variable bunch compressors, *Phys. Rev. Accel. Beams* 27, 110702, 2024.